Influenza causes alterations to oligodendrocyte-specific transcripts and the myelin lipidome in the adult mouse central nervous system.

Allison Louie
University of Illinois at Urbana-Champaign
Justin Kim
University of Illinois at Urbana-Champaign
Katiria Soto-Diaz
University of Illinois at Urbana-Champaign
Payam Dibaeinia
University of Illinois at Urbana-Champaign https://orcid.org/0000-0003-2978-2520
Hisami Koito
Josai University
Saurabh Sinha
University of Illinois at Urbana Champaign https://orcid.org/0000-0001-6033-7746
Romana Nowak
University of Illinois at Urbana-Champaign
Aditi Das
University of Illinois at Urbana Champaign https://orcid.org/0000-0002-6731-6726
Andrew Steelman (asteelma@illionis.edu)
University of Illinois at Urbana-Champaign

Article

Keywords: myelin plasticity, remodeling, lipidome, oligodendrocyte, influenza, systemic infection

Posted Date: March 22nd, 2021

DOI: https://doi.org/10.21203/rs.3.rs-310861/v1

Abstract

The notion that myelin remains static during adulthood has been challenged in recent years. Myelin is not only crucial for proper cognitive function and behavior, but it is vulnerable to alterations from external factors outside the window of development. Here, in the adult mouse CNS, RNA analysis revealed global downregulation and subsequent recovery of oligodendrocyte-specific transcripts in response to peripheral influenza viral infection. Furthermore, shot-gun lipidomic analysis revealed that infection alters the lipid profile in the prefrontal cortex as well as in purified brain myelin. Finally, treatment with the colony stimulating factor receptor (CSFR)1 antagonist GW2580 during infection suppressed glial activation and partially restored oligodendrocyte-specific myelin transcripts to baseline levels. Together, these findings reveal a yet unforeseen consequence of peripheral infection on oligodendrocyte homeostasis in the adult mouse.

Introduction

Myelin, the fatty, insulating substance that constitutes brain white matter, forms compact concentric sheaths around axons, increasing neuronal conduction velocity by 10-100-fold at a fraction of the energy demand[1,2]. In the central nervous system (CNS), oligodendrocytes (OLs) are responsible for internodal myelin segment formation. Myelin is required for proper motor function and is imperative for higher order cognition, such as reading, vocabulary and executive decision-making[3,4]. In contrast, hypomyelination and demyelination are pathological features of a myriad of neurological diseases. White matter abnormalities are observed in schizophrenia[5-7], cognitive decline due to aging[8], Alzheimer's disease[9], multiple sclerosis[10] and depression[11].

While it has been known for some time that alterations in OL homeostasis affect cognition and behavior, the notion that myelin remains static during adulthood has only recently been challenged. Evidence implicating myelination as an ongoing and dynamic process is illustrated by the findings that changes to white matter structures occur when learning complex motor skills such as playing an instrument[12] or juggling[13]. Myelin is also affected by other environmental factors such as diet, exercise, and the microbiome[14]. Importantly, Yeung et al. found that even though the turnover of OLs is slow, myelin itself is continuously exchanged[15]. Interestingly, OLs have the capacity to completely renew myelin membranes up to three times in one day[16], a finding corroborated by studies in zebrafish demonstrating the capacity for OLs to make new myelin sheaths in five hours[17].

While structural integrity of myelin can be attributed to proteins such as myelin basic protein (MBP)[18], proteolipid protein (PLP)[19], or apolipoproteins[20], the interaction between lipids within the myelin sheath also contribute to the formation and function of myelin. Lipidomics has emerged as a powerful tool with which to elucidate changes to the lipid species of myelin[21]. Since both the structure and biochemical profile of myelin affect conduction velocity, alterations to myelin thickness, length, or lipid composition might affect neurocircuitry, modulate synaptic plasticity, and influence behavior. Alterations in the lipid

profile alone can result in ultrastructural changes to myelin[22], and deletion of particular lipid species of myelin can have functional consequences on conduction velocity despite overall normal-appearing structure[23,24]. However, the influence of environmental factors on the myelin lipidome has not yet been elucidated.

Systemic inflammation induces behavior modifications that mimic those following perturbations to myelin[25]. For instance, patients with severe respiratory infections caused by influenza or SARS viruses can develop encephalopathy characterized by confusion, depressed mood, anxiety, impaired memory, insomnia, mania and psychosis even in the absence CNS invasion[26,27]. In survivors, these manifestations may be long lasting[27,28]. While the underlying factors dictating these behavior changes are unknown, they are thought to involve high levels of systemic inflammation. It is known that microglia become reactive in response to systemic inflammation[29] or viral infection[30-32] and that this phenomenon is correlated to altered behavior. Microglial reactivity is also a prominent feature of most white matter diseases and the proinflammatory cytokines they produce during systemic inflammation influence OL homeostasis[33]. Whether aberrant inflammation brought on by viral infection alters myelin plasticity in adults has not yet been investigated. Since both proteins and lipids contribute to the structure and thus function of myelin, in the current study, we comprehensively examine how systemic inflammation influences both the transcriptional and the biochemical profile of myelin. Here, we report that respiratory infection with influenza virus suppresses OL-specific transcription and alters the lipid profile of myelin in the adult mouse CNS.

Results

Transcripts associated with myelination are temporally suppressed by influenza infection.

We recently demonstrated that influenza infection, while confined to the lung, altered the cerebellum and spinal cord transcriptome[34]. Here, using a threshold FDR<0.05, we identified 2093 downregulated genes in both cerebellum and spinal cord tissues of influenza-infected mice compared to saline-inoculated controls at day 8 post-infection (p.i.) (Fig. 1a). Gene ontology (GO) enrichment analysis revealed these downregulated genes were associated with 63 GO terms shared between both tissues (Fig. 1b). The most highly enriched terms included *myelination*, *cholesterol biosynthetic process*, *phospholipid biosynthetic process*, and *sphingolipid biosynthetic process*, indicating these lipid biosynthesis pathways might be impaired as a result of influenza infection (Fig. 1c). The downregulation of these pathways is of great interest given that the major lipid classes of myelin are 1) cholesterol, 2) phospholipid, including plasmalogen, phosphatidylcholine (PC), and sphingomyelin (SM), and 3) glycolipid, including glycosphingolipids such as glucosylceramide (CerG) and sulfatide[35] (Fig. 1d). Indeed, expression of multiple enzymes that are essential for cholesterol biosynthesis including *Dhcr7*, *Hmgcr*, and *Fdft1* was decreased in spinal cord and cerebellum tissues of infected mice (Fig. 1e). Likewise, gene expression of several families of lipids involved in phospholipid biosynthesis such as lysophosphatidic acid acyltransferases (*Agpat*) and phosphatidylinositol glycan anchor synthases (*Pig*) as well as in

glycosphingolipid biosynthesis such as long-chain fatty acid elongases (*Elovl*) and 3-hydroxyacyl-CoA dehydratases (*Ptpla*) was downregulated in both CNS tissues in response to infection (Fig. 1e). In addition to these lipid biosynthetic enzymes, genes encoding myelin proteins such as *Mag*, *Mog*, and *Plp1* were downregulated in both CNS tissues. Taken together, these results indicate that infection may act to globally suppress the transcription of genes involved in lipid biosynthesis and myelination.

To validate these results and characterize any regional differences in transcription, we repeated the experiment and measured expression of select myelination genes in the medial prefrontal cortex (mPFC), cerebellum, and hippocampus by RT-qPCR (Fig. 2a). By day 8 p.i. infected mice exhibited maximal weight loss (Fig. 2b). At this time point, we found that expression levels of *Plp1*, *Mag*, and *Mog* were suppressed in cerebellum, mPFC, and hippocampus (Fig. 2c). Additionally, *Mbp*, *Cnp*, and *Ugt8a* were suppressed in the hippocampus (Fig. 2c). These data substantiate our previous findings and indicate that influenza infection decreases transcription of OL-specific genes in multiple regions of the brain. By day 16 p.i., body weights returned to baseline, indicating that the mice were recovered (Fig. 2b). OL-specific genes also returned to baseline levels of control mice in the mPFC and hippocampus (Fig. 2c). Interestingly, *Plp1* and *Mog* were still downregulated in the cerebellum (Fig. 2c).

Influenza infection does not significantly alter PLP levels in the mPFC.

Proteolipid protein (PLP) is the most abundant protein of myelin and is necessary for healthy, compact myelin as it preserves myelin stability and integrity and prevents axonal pathologies[36,37]. Since *Plp1* expression was decreased in all regions examined as a result of infection, we sought to determine if there were overt changes to protein expression within the mPFC. Typically, it is challenging to quantify gray matter PLP levels in an unbiased fashion due to the dense packing of fine, intricate strands of white matter. But, along with the important behavioral implications of the prefrontal cortex, evaluation of myelin in this region is advantageous in that it allows for measuring attributes of many individual myelinated axons across a large area as opposed to whole white matter tracks where very minor alterations to myelin protein might go unnoticed. Thus, to obtain unbiased quantitative measures of PLP on a large but sensitive scale, we utilized CLARITY tissue-clearing and confocal microscopy to stain and image large areas (850x850x100 μm) of the adult mouse mPFC. Three dimensional (3D) models of the resulting PLP scaffold of the myelinated fibers were created and analyzed using Imaris software (Fig. 3a). To ensure changes to myelin could be detected by our method as well as to identify which output measures from Imaris indicated changes to myelin, we analyzed mPFC tissue of mice after 5 weeks of cuprizone intoxication, which is known to cause demyelination in this region[38]. The resulting 3D models of the three treatment groups (Fig. 3b) produced quantifiable attributes related to myelinated fibers such as filament diameter and volume (Fig. 3c). Definitions of measures generated by Imaris and corresponding data are published as supporting information (Supplementary Data 1, Supplementary Table 6). Compared to saline control mice, cuprizone-fed mice had smaller values for mean filament diameter, a reflection of myelin thickness, as well as total filament volume, which is indicative of total myelin. However, of the 19 measures analyzed, we found no significant differences between the saline- and flu- inoculated mice at

day 8 p.i. This suggests that influenza infection does not considerably alter the levels of PLP in adult myelin, despite the decrease in myelin gene transcripts.

Influenza infection alters the myelin lipidome.

We showed that OL-specific genes were downregulated in the mPFC at day 8 p.i., with a recovery in expression at day 16 p.i. Therefore, we sought to determine if there were any lipidome changes in mPFC due to influenza infection. We isolated the mPFC from saline or infected mice at day 8 and day 16 p.i. In total, 1091 lipid species belonging to 28 major lipid classes were identified in the mPFC. Three pair-wise comparison analyses were conducted in the following manner: A) Saline vs. Flu Day 8, B) Saline vs. Flu Day 16, and C) Flu Day 8 vs Flu Day 16. In the mPFC at day 8 compared to saline, there were a total of 215 lipid species that were differentially expressed (Fig. 4a). While a majority of the major lipid classes increased in Flu Day 8 of the mPFC, three lipid species belonging to So and TG classes were decreased. On Flu Day 16 of the mPFC 338 lipid species belonging to 25 major lipid classes were differentially expressed (Fig. 4b). Interestingly, the only major lipid class that was not increased in Flu Day 16 of the mPFC was cholesterol. When comparing Flu Day 8 to Flu Day 16, there were minimal differences (Fig. 4c). Specifically, there were only 16 lipid species that were differentially expressed. These data indicate that modulation of lipids by infection does not recover to baseline levels by day 16 p.i., despite recovery of gene expression and body condition score.

To further assess the effects of upper-respiratory infection on myelin, we isolated purified myelin from the whole brain for lipidomic analysis. Myelin was purified from whole mouse brain by density gradient fractionation and osmotic shock. Myelin enrichment was verified by SDS-PAGE and western blot, which confirmed abundant PLP and negligible levels of the astrocyte protein glial fibrillary acidic protein (GFAP) in extraction myelin fractions (Supplementary Figure 4). A total of 176 lipid species were differentially expressed out of 1356 total lipid species identified (Fig. 4d). With the exception of LPA, LPS, and PEt which decreased by nearly 2-fold, most of the affected lipid classes were increased in flu-inoculated mice compared to saline controls at day 8 p.i. These data corroborate the lipidomic findings in the mPFC, where lipid species are greatly increased as a result of infection.

In addition to the increase of major lipid classes that are differentially expressed in flu-infected mice, there are other underlying similarities. For instance, lipids that are known to be involved in the structural integrity of myelin including Cer, CerG, PE, PC, SM and So are all differentially expressed in both mPFC and myelin isolated from the whole brain. Therefore, we conducted bioinformatic analysis using LIPEA. Following Bonferroni correction, we discovered that glycerophospholipid metabolism and sphingolipid signaling pathways were the most highly enriched (Fig. 5). Collectively, these data demonstrate that influenza infection results in alterations of the myelin lipidome.

Infection-induced changes to OL-specific transcripts are associated with glial activation and are partially attenuated following systemic treatment with a CSF1R antagonist.

Our results strongly suggest that influenza infection altered OL homeostasis. We, and others, have previously shown that influenza infection is associated with glial activation[30-32,34]. However, how resident CNS cell populations, at scale, are affected by influenza viral infection is not known. Therefore, we next performed a scRNA-seq experiment on cells isolated from saline and influenza infected mice at day 8 p.i. to determine which glial cells were activated. In total we sequenced 4,142 cells from saline and infected mice. Using cell-specific transcripts from published data bases we identified astrocyte, microglia, epithelial cells, endothelial cells, neurons, myeloid cells and OLs (Fig. 6a). Infection profoundly affected the transcriptome of each of these cell subsets (Fig. 6b), as indicated by gene ontology analyses performed on differentially expressed genes (Supplementary Figures 1-2).

Transcriptomic changes were especially apparent for microglia, astrocyte, and epithelial cell populations. We had previously observed changes to genes that are indicative of proinflammatory reactive astrogliosis ('A1') that have been described as both damaging to OLs and neurotoxic[34,39]. Since this astrocyte phenotype is dependent on microglia TNF, IL-1α and C1q production we determined if the genes encoding these proteins were induced by infection. The percentage of microglia that upregulated *Tnf* and *Il1a* was increased in infected mice. However, microglia constitutively expressed high levels of *C1qa*, a finding that we confirmed using both Brain-RNAseq[40], the Allen Brain Atlas[41] and *Tabula muris*[42] references. We next questioned whether infection affected transcription of genes associated with astrocyte reactivity. The percentage of astrocytes expressing ≥1 marker of 'Pan' reactivity was increased in infected mice (62.39%) compared to controls (19.38%). Similarly, the percentage of astrocyte expressing ≥1 marker of 'A1' astrocyte reactivity was increased in infected mice (67.4%) compared to controls (25.85%). The percentage of astrocytes expressing ≥1 marker of 'A2' astrocyte reactivity in infected mice (21.53%) compared to controls (18.0%) was comparable. It is noteworthy that many other cell types, including microglia, express genes associated with 'A1' and 'A2' astrocyte reactivity during infection. Therefore, we sought out upregulated genes that were predominantly restricted to microglia, astrocytes, or that were indicative of reactivity across cell types in order to use them as surrogate markers for subsequent studies. Our analyses indicated *Tnf, Mfsd2a* and *Cdkn1a* may prove efficacious as potential markers of microgliosis, astrogliosis and pan reactivity, respectively, following influenza infection (Fig. 6c-d).

We questioned whether inhibiting microglia activation might reverse the effect of infection on the transcriptomic changes that occur to OLs. Microglia activation, proliferation and survival are, in part, contingent on constitutive colony stimulating factor receptor (CSF1R) signaling. In fact, oral treatment with the CSF1R inhibitor GW2580 inhibits disease progression in animal models of multiple sclerosis[43], amyotrophic lateral sclerosis[44], Alzheimer's disease[45], promotes recovery after spinal cord injury[46], mitigates chronic inflammation associated pain[47], and attenuates depression-like behavior in MRL/lpr mice[48] without affecting microglia viability[45]. Notably, analysis of bulk-seq from cerebellar tissue indicated that *Csf1* was increased at day 8 p.i., whereas expression of *Il34* was unchanged (Supplementary Figure 2). Furthermore, *Csf1r* expression of infected mice was increased at day 4 p.i. and decreased at day 8 p.i. compared to saline-inoculated controls (Supplementary Figure 2). Analysis of our scRNA-seq data set confirmed these findings, in that we found the percentage of microglia and astrocytes

expressing *Csf1* was elevated by infection (Supplementary Figure 2). *Il34* transcripts were detectable in endothelial cells and neurons but were not affected by infection (Supplementary Figure 2). The expression of *Csf1r*, the receptor for both CSF1 and IL-34, was largely restricted to *Tmem119*-expressing microglial cells. Therefore, we questioned whether treatment with GW2580 alleviated changes to OL transcripts resulting from influenza infection. Treatment did not affect recruitment of $CD45^+$ myeloid cell subsets to the lung at either day 8 or day 16 p.i. (Supplementary Figure 2). As before, infection increased expression of *Tnf* and *Cdkn1a* in the mPFC, cerebellum and hippocampus, but *Mfsd2a* expression was only increased in the mPFC (Fig. 6e). Treatment with GW2580 had the most dramatic effect on *Tnf*, as it appeared to lower *Tnf* expression in the mPFC, cerebellum and hippocampus. However, the effect of treatment was only significant for the mPFC (Fig. 6e). As observed in our previous experiments, infection decreased transcription levels of OL-specific genes *Plp1*, *Ugt8a* (Fig. 6f) and *Mag* (Supplementary Figure 3). Interestingly, treatment with GW2580 tended to increase the expression levels of myelin genes, an effect that was significant in both the hippocampus and cerebellum (Fig. 6f). Collectively, these data show influenza infection promotes glial reactivity which coincides with the suppression of genes that encode proteins that are involved in myelin maintenance. Moreover, antagonism of microglial CSF1R partially inhibits glial reactivity and in part reverses changes to OL-specific transcripts.

Discussion

In the current study, we investigated the effect of infection on OL homeostasis. We found infection invoked widespread downregulation of transcripts involved in myelination in the adult mouse CNS. The effect of infection on the OL transcriptome was reversed by day 16 p.i. in the mPFC and hippocampus. Moreover, we found that infection caused changes to the myelin lipidome. These changes were predominately characterized by upregulation of SM, Cer and CerG, but also entailed downregulation of the LPA, LPS, and PEt lipid classes. Finally, infection increased gliosis and systemic treatment with a CSF1R antagonist partially reversed the effect of infection on OL-specific transcripts. To our knowledge, this is the first study to demonstrate that respiratory viral infection is capable of facilitating global transcriptomic and lipidomic changes to OLs and myelin, respectively.

In recent years, it has become clear that myelin is dynamic and subject to remodeling even in adulthood[15,49,50]. Myelin can be remodeled by environmental factors such as learning a new task[12,13], social isolation and reintegration[51], and by social defeat stress[52,53]. Stress is considered a potent risk factor for the onset of depression and mood disorders[54]. In socially-isolated or stressed mice, OL and myelin transcripts were decreased in the prefrontal cortex[51,52,55], a region that is compromised in depression and other disorders associated with white matter abnormalities. Moreover, transcriptomic analysis of brains from healthy controls vs. people suffering from major depressive disorder revealed suppression of multiple genes involved in myelination. These genes included: *UGT8, PLP1, CNP, MAG, MAL, MOG, MOBP, PMP22, PLLP, ASPA, ENPP2, EDG2, TF* and *KLK6*[56]. Notably, bulk-seq analysis of cerebellar tissue from infected mice revealed nearly all of these genes (13/14) were suppressed eight days after infection compared to control mice[34]. Here, we extend these findings and show that myelin

and cholesterol biosynthesis transcripts were decreased in the mPFC, cerebellum, and hippocampus of infected mice. Depression is highly comorbid with several inflammatory disorders[57] and neuroinflammatory events influence depression pathology[58]. It is notable that, depression and systemic infection share many of the same symptoms such as lethargy, anhedonia, and social isolation[59]. It is plausible that the transcriptional effects observed in response to influenza infection and those observed in mice exhibiting depressive-like behavior after subjection to experimental stressors can be attributed to the same causal pathway involving activated glia. We recently reported that influenza infection upregulated expression of genes in the cerebellum and spinal cord that were associated with activated glial phenotypes and under the putative regulatory control of interferon (IFN) activated transcription factors[34]. Since IFN transcripts were not detectable in the transcriptome, we hypothesized that the actions of IFN were a result of peripheral upregulation. With this in mind, it is notable that IFN treatment in patients with chronic Hepatitis C virus is associated with a high incidence of depression[60] and that deletion of IFN receptor chain 1 (IFNAR1) ameliorates sickness behaviors resulting from experimental viral infection[61]. As such, interferon(s) may act independently or in concert with other inflammatory mediators to affect myelin plasticity.

Interestingly, despite the transcriptional changes to myelination genes, there were no changes to the myelin protein PLP in the prefrontal cortex as observed by immunofluorescence. Given that the half-life of PLP in the adult mouse is estimated to be 6 months[36], it is reasonable to conclude that downregulation of *Plp1* does not immediately translate into significant changes to PLP in infected mice at day 8 p.i. Furthermore, PLP as well as MBP are major constituents of compact myelin, which turns over at a slower rate than noncompact myelin[62]. In the chronic social defeat stress model, there are some conflicting reports describing either no difference in levels of MBP in the mPFC between groups[53] or decreased levels of MBP in the mPFC of stressed mice[52]. Given the slow turnover of myelin proteins, this discrepancy may also have been influenced by volume of tissue analyzed or time of sacrifice. Nevertheless, data generated from the current set of experiments underscore the need to evaluate both the structural and biochemical aspects of myelin for a comprehensive understanding of how environmental factors might contribute to myelin remodeling.

By lipidomic analysis, we found that 13% of total lipid species identified were affected by influenza infection, the majority of which were upregulated. Although RNA analyses revealed the transcription of genes involved in lipid biosynthetic pathways was downregulated, it is important to recognize that lipids are often short-lived and precursors are continuously recycled. Thus, downregulation of an enzyme involved in a lipid biosynthetic pathway may in fact cause a bottle-neck accumulation of certain lipid substrates. This hypothesis is supported by data that demonstrate brain ceramide levels are increased in mice that completely lack *Ugt8a* as well as in those in which *Ugt8a* is conditionally deleted in oligodendrocytes, while glycolipids (i.e. galactosylceramide) and sulfatide are diminished[63]. Furthermore, in the same study, mass spectroscopy analysis performed on *Ugt8a* mutants indicated that *Ugt8a* mutant mice have an approximate 20% increase in phosphatidylethanolamine, phosphatidylserine and

phosphatidylcholine. As such, suppression of *Ugt8a* by infection might promote accumulation of ceramide and sphingomyelin species.

We observed changes in PC, which aligns with previous studies demonstrating that schizophrenic patients have dysregulated levels of PC in gray matter[64]. Furthermore, it has been shown that PC and PEt plasmalogens were increased in the frontal cortex in Alzheimer's patients[65]. Despite these trends, there are some conflicting data in the field. In contrast to previous studies, others have shown a decrease in PC and PEt lipids in the prefrontal cortex in patients with cognitive disorders[66]. As such, further investigation will be needed to fully elucidate the specific role of lipids in behavioral and cognitive function. Nevertheless, our data clearly demonstrate the capacity for influenza infection to alter the myelin lipidome.

While shotgun lipidomics have advantages of high throughput, it is difficult to delineate isobars[67]. Additionally, several other critical lipids such as cholesterol that are often stored in their esterified form in the membranes cannot be detected without de-esterification process that might cause other changes in the lipids extracted from the myelin of mice. Our results align with previously published work, indicating that myelin extraction from 8-10 week old mice analyzed via LC-MSMS does not yield high levels of cholesterol[68].

While there are some caveats to scRNA-seq data-sets, such as overrepresentation or exclusion of cell types (i.e. OLs vs. microglia) as well as small sample size, our data were well aligned with previous bulk-seq experiments. Data generated by our scRNA-seq experiment outlines changes that occur to specific glial and neuronal subsets during systemic inflammation. These data also identified the CSF1-CSF1R axis as a potential target for controlling microglia activation in response to systemic inflammation, and thus provided the basis for assessing a CSF1R antagonist on transcriptomic changes to OLs. That influenza-induced changes to OL-specific transcripts were partially reversed by antagonizing CSF1R implicates a role for activated $CSF1R^+$ microglia in this process. Since microglia were not deleted by treatment, it is possible, albeit unlikely, that microglia activation accounts for all changes to OL homeostasis either directly or indirectly through astrocyte activation. Importantly other contributing factors resulting from infection likely influence glial responses. For instance, hypoxemia is known to affect developing OLs[69,70]. Possible underlying processes are enhanced systemic inflammation and increased oxidative stress that can also occur under hypoxic conditions caused by acute respiratory infection. In this manner, hypoxia may have contributed to infection-induced alterations of white matter in the current set of experiments. The contribution of these factors on OL homeostasis are the subject of current investigation.

In conclusion, our results demonstrated that peripheral infection with influenza A virus globally altered the OL transcriptome and myelin lipidome in the adult mouse CNS with partial reversal of OL transcript changes by a CSF1R antagonist. Overall these observations improve our understanding of the capacity of peripheral infection to contribute to myelin remodeling.

Materials And Methods

Animals and viral infection

Male C57BL/6J mice were obtained from Jackson Laboratories (No. 000664). Animals were housed 4-5 per cage under constant 12-h light/dark cycles (10am-10pm) and constant temperature and fed a standard rodent diet (Envigo Diet No. 2918) *ad libitum*. Mice (aged 8-11 wk) were anesthetized with 3% isoflurane and then inoculated with either sterile saline or one haemagglutination unit (HAU) of mouse-adapted human influenza A virus (strain A/Puerto Rico/8/1934 H1N1) diluted in sterile phosphate buffered saline (PBS). The total inoculation volume was 30 µl. Animals were weighed daily and then euthanized by CO_2 asphyxiation at days 8 and 16 p.i. for follow-up experiments. Weight data were pooled from all experiments. All animal care protocols were in accordance with National Institutes of Health Guidelines for Care and Use of Laboratory Animals and were approved by the University of Illinois Laboratory Animal Care and Use Committee.

RNA-sequencing

In the current study, we provide an extensive analysis of down-regulated genes in the cerebellum and spinal cord of influenza inoculated mice using a data-set that we have previously published[34]. The RNA sequencing datasets associated with this paper have been deposited into the Gene Expression Omnibus database (https://www.ncbi.nlm.nih.gov/geo/) and can be accessed using the accession no. GSE96870. Gene ontology and pathway analyses were performed on downregulated genes that achieved a P-value<0.05 and FDR<0.05 using DAVID Bioinformatics Resources 6.8 (https://david-d.ncifcrf.gov/). For single-cell (sc)RNA-sequencing female mice were inoculated with saline (n=1) or influenza (n=1; 1.0 HAU). After 8 days, the mice were euthanized then perfused through the heart with 20 ml of ice cold artificial cerebrospinal fluid then the brain extracted. The brain whole brain was dissociated and vial single cell suspensions prepared using a MACS dissociator (Milltyni) using neural dissociation, debris/myelin removal and dead cell removal kits according to the manufacturer's instructions (Milltyni). Viable cells, determined to be greater than 80% of the cell population. In total 3000 viable cells were targeted per condition for library preparation. Libraries prepared using the Chromium^{TM} Single cell 3’ Library & Gel Bead kit v2 (10X Genomics) then sequenced on two 150nt lanes using an Illumina Hiseq 4000. Sequences were then demultiplexed using the mkfastq option from Cell Ranger 2.1.1 and analyzed in Loupe Browser. The estimated number of cells sequenced were 1,894 and 2,248 for saline and influenza infected mice respectively. The mean reads per cell were 185,309 (saline) and 151,067 (infected) with 87.5% (saline) and 85.9% (infected) confidently mapped to the genome. The median number of genes per cell were 1,770 and 1,519 for saline and influenza infected mice respectively.

Single cell (sc)RNA sequencing analysis

Data analysis was performed using Loupe Cell Browser (10X Genomics), which creates cell clusters based on transcriptional similarity and t-SNE plots created. Cell subsets were identified using *Tmem119* as a marker for microglia, *Aqp4* for astrocytes, *Cldn5* for endothelial cells, *Igf2* for epithelial cells, *Ptprc* for myeloid cells and *Sp9* for neurons. Significant up and downregulated genes were identified using the Loupe 10X genomics server and then gene ontology was used to characterize the gene functionality. Microglia glia activation was determined by looking at *Tnf*, *Il1a* and *C1qa* gene expression. Reactive astrocyte subpopulations were identified using transcriptional markers previously described[39]. Specifically, within the *Aqp4*$^{+}$ populations 'PAN'-reactive astrocyte populations were identified by the presence of *Lcn2*, *Steap4*, *S1pr3*, *Timp1*, *Hspb1*, *Cxcl10*, *Osmr*, *Cp*, *Aspg*, *Gfap*, and/or *Vim* gene expression; 'A1' reactive astrocytes were identified by the presence of *H2-D1*, *Serping1*, *H2-T23*, *Ggta1*, *Iigp1*, *Gbp2*, *Fkbp5*, *Psmb8*, *Srgn*, and/or *Amigo2* gene expression. Finally 'A2' reactive astrocytes were identified by the presence of *Clcf1*, *Ptx3*, *S100a10*, *Cd109*, *Ptgs2*, *Emp1*, *Slc10a6*, *Tm4sf1*, *B3gnt5* and *Cd14* gene expression.

Tissue extraction and gene expression by RT-qPCR

Mice were euthanized at days 8 and 16 p.i., brains were harvested, bisected, and immediately placed in RNALater (Thermo Scientific Cat No. AM7020) at 4°C for 24-48 hours and then stored at -80°C for later use. The medial prefrontal cortex (mPFC), cerebellum, and hippocampus were hand-dissected with the aid of a dissection microscope (Leica). The RNA from each brain region was isolated using TRIzol Reagent (Thermo Scientific Cat. No. 15596018) according to manufacturer's instructions and purified using GeneJET RNA purification kit (Thermo Scientific, Cat. No. K0731). cDNA was obtained using the Reverse Transcription System (Promega Cat. No. A3500) according to manufacturer's instructions in a C1000 Touch Thermal Cycler (Bio-Rad Laboratories). Relative gene expression of select downregulated genes as indicated by RNA-sequencing results was determined using TaqMan Gene Expression Probe Assays (Integrated DNA Technologies, SI Table S1) on a QuantStudio 7 real time PCR system (Applied Biosystems, Thermo Scientific). All samples were run in duplicate. Expression levels were calculated as the average of two replicates for each biological sample from both groups (n=3-7 animals per group) relative to β-actin expression. Fold change was calculated using the formula $2^{-\Delta\Delta Ct}$.

Cuprizone model

Male C57Bl/6J mice (aged 8 wk) were fed 0.2% cuprizone-laced diet (Envigo Diet No. 140800) for 3 weeks to induce demyelination[71], followed by 2 weeks of normal rodent diet. Mice were sacrificed at 5 weeks post-cuprizone during maximal demyelination phase for subsequent CLARITY tissue processing.

CLARITY tissue processing and immunostaining

Mice were euthanized at day 8 p.i., brains were harvested, bisected, and post-fixed in PBS containing 4% PFA (w/v) overnight at 4°C. Halved brains were then incubated in PBS overnight at 4°C. Next, 1mm sagittal sections were generated using a sagittal mouse brain matrix (Kent Scientific). Each section was then submerged in hydrogel solution (modified from Epp et al., 2015)[72] containing final concentrations of 3% acrylamide (Bio-Rad Cat. No. 161-0140), 3% formaldehyde (Electron Microscopy Sciences Cat. No. 19200), and 0.25% VA-044 thermal initiator (m/v; Wako Chemicals Cat. No. NC0632395) for 24-48 h at 4°C. Incubated tissues were polymerized in hydrogel solution at -90kPa for 3 h at 37°C, washed three times with PBS, then actively cleared by electrophoresis using X-CLARITY^{TM} Tissue Clearing System (Logos Biosystems). After washing overnight in PBS to remove any residual SDS, the tissues were incubated in PBS containing anti-proteolipid protein (PLP) (clone AA3; hybridoma solution diluted 1/20), 0.1% Triton-X 100 (v/v; Sigma Aldrich Cat. No. T8787; PBST), 2% goat serum (Abcam Cat No. ab7481), and 0.01% sodium azide (Sigma Aldrich Cat. No. S2002) for 3 days at 50 rpm and 37°C in an orbital shaker (Thermo Scientific Max Q 4000). After washing for 24 h in PBST, tissues were stained with goat anti-rat IgG (H+L) cross-adsorbed Alexa Fluor 594 secondary antibody (diluted 1:100 in PBST, Thermo Scientific Cat. No. A-11007) under the same conditions as the primary step and subsequently washed for 24 h in PBST. Tissues were then incubated in X-CLARITY mounting solution (RI=1.46, Logos Biosystems Cat. No. C13101) for 24-48 h before mounting between coverslips (Thermo Scientific Cat. No.) using iSpacers® (SunJin Lab).

Imaris 3D modeling and analysis

Sets of 100 serial images at 1 µm steps in the Z direction, 0.48µm/pixel in the X, Y-plane, and 0.95 µsec pixel dwell time were acquired with the Zeiss LSM 710 Confocal Microscope and 10x objective, resulting in whole datasets of 850x850 µm in the X, Y-plane and 100 µm in the Z direction. Three-dimensional (3D) images were rendered with Imaris 9.3 software (Bitplane, Oxford Instruments) and analyzed with the software's automated Filament Tracer module. 3D animations were created with the Animation Feature of Imaris. All images were analyzed in the same fashion by a rater blinded to condition.

Myelin extraction

Animals were euthanized via CO_2 asphyxiation and perfused with PBS. Whole brains were harvested and flash frozen under liquid nitrogen within 2 minutes of euthanasia. Myelin was extracted from brains under sucrose density centrifugation and osmotic shock as previously described[73]. All solvents were prepared fresh at 4°C, and extractions conducted under ice. Additionally, all extractions were conducted using the same solvents on the same day. Briefly, brains were homogenized with a dounce homogenizer in 0.3 M sucrose containing 0.7 M Tris-HCl (pH 7.4), 10 µg/mL Leupeptin (Sigma Aldrich, No. 103476-89-

7), 10 µg/mL Antipain (Sigma Aldrich, No. 37691-11-5), and 100 µM phenylmethylsulfonyl fluoride (GoldBio, No. P-470). Homogenized brain samples were layered on 0.83 M sucrose containing Tris-HCL, leupeptin, antipain and phenylmethylsulfonyl fluoride (PMSF). The dounce homogenizer was washed twice with 0.3 M sucrose and additionally layered. Samples were centrifuged for 30 m at 75,000 xg, 4°C, and without brakes to prevent disruption of density gradient layers. Following centrifugation, the crude myelin interface between 0.83 M sucrose and 0.3 M sucrose was collected and transferred to a new centrifuge tube containing MQ H_2O for centrifugation at 75,000 xg, 4°C for 30 m. Osmotic shocks were then conducted twice by resuspending myelin in 5 mL MQ H_2O and homogenizing thoroughly. Following a 10 m incubation on ice, samples were centrifuged for 15 m at 12,000 xg, 4°C and without brakes. After two osmotic shocks, pelleted crude myelin was resuspended in 2 mL 0.83 M sucrose and layered on 16 mL 0.83 M sucrose, followed by a 0.3 M sucrose. The samples were centrifuged for 15 m at 75,000 xg, 4°C and without brakes. The interface was then transferred to a new tube and resuspended in MQ H_2O for final centrifugation at 75,000 xg, 4°C and without brakes. The supernatants were carefully discarded to obtain the purified myelin. The purified myelin was then resuspended in 100 µL 1 M Tris-HCl and stored in -80°C.

Lipid extraction

Total lipids were extracted from purified myelin using the Bligh & Dyer method[74]. Briefly, extracted myelin sheath samples were added to 750 µL 1:2 $CHCl_3$:MeOH and vortexed for 15 m at 25°C. Following 5 m incubation on ice, 250 µL $CHCl_3$ and 250 µL MQ H_2O were added to the sample. Samples were then vortexed for 5 m at 25°C, and centrifuged for 5 m at 800 xg at 4°C. The organic layer was collected and dried under steady flow of N_2 gas and resuspended in 90% ethanol for analysis via LC-MSMS.

Lipidomics

The samples were spiked with 5 µL of 50 µg/mL internal standard mixture (Ceramide 18:1/12:0; Phosphatidylcholine 12:0/12:0; Phosphatidylethanolamine 14:0/14:0; phosphatidylglycerol 14:0/14:0; phosphatidylserine 14:0/14:0) before instrument injection. The samples were analyzed at the Metabolomics Laboratory of the Roy J. Carver Biotechnology Center of the University of Illinois at Urbana-Champaign. Samples were injected into the Dionex Ultimate 3000 series HPLC system (Thermo Scientific, Germering, Germany) which included an autosampler, degasser, and a binary pump. Liquid chromatography separation was conducted on a Thermo Scientific Accucore C18 column (2.1x150 mm, 2.6 µm) with a flow rate of 0.4 mL/min. Mobile phase A (60% acetonitrile: 40% H_2O containing 10 mM ammonium formate and 0.1% formic acid) and mobile phase B (90% isopropanol: 10% acetonitrile containing 10 mM ammonium formate and 0.1% formic acid) was utilized. The detailed method was similar to previously published paper from the laboratory[75]. The following linear gradient was used: 0

min, 70% A; 4min, 55% A; 12 min, 35% A; 18 min: 15% A, 20-25 min: 0% A, 26-33 min: 70% A. The injection volume was 10 µL, autosampler was set to 15°C, and column was kept at 45°C. Thermo Scientific Q-Exactive MS system (Bremen, Germany) was used for obtaining tandem mass spectrometry under both positive (sheath gas flow rate, 50; aux gas flow rate, 13; sweep gas flow rate, 3; spray voltage, 3.5 kV; capillary temp, 263°C; aux gas heater temp, 425°C) and negative electrospray ionization (sheath gas flow rate, 50; aux gas flow rate, 13; sweep gas flow rate, 3; spray voltage, -2.5 kV; capillary temp, 263°C; aux gas heater temp, 425°C). The full scan mass-spectrum resolution was set to 70,000 resolution at *m/z* 200 with scan range of *m/z* 230-1,600. The automatic gain control target was 1,000,000 using the maximum injection time of 200 ms. For MSMS, the mass spectrum resolution was set to 17,500. The automatic gain control (AGC) target was 50,000 with a maximum injection time of 50 ms. Loop count was 10. Isolation window was *m/z* with normalized collision energy (NCE) of 25 and 30 eV.

GW2580 treatment

C57BL/6J mice were housed in reverse light-cycle conditions and were fed a diet of normal chow and water consumption *ad libitum* prior the treatment. Mice were treated daily with GW2580 (80mg/kg/d; LC Labs, Cat No. G-5903) diluted in 200µl of 0.1% Tween80, 0.5% Hydroxymethyl Propyl-cellulose or vehicle alone by oral gavage using plastic feeding tubes (Instech, FTP-18-30-50). Treatment began seven days prior to inoculation with saline or influenza and continued for the duration of the study (to day 8 p.i.). In total mice were treated for fifteen days. Animal weights were recorded daily.

Serial block face scanning electron microscopy and g-ratio analysis

Immediately upon dissection, prefrontal cortex tissue was drop-fixed in 0.15M sodium cacodylate buffer containing 2.5% glutaraldehyde and 2% formaldehyde with 2mM calcium chloride (pH 7.4). Tissue was then post fixed in 2% osmium tetroxide in 0.15 M cacodylate buffer and 1% thiocarbohydrazide solution. Tissues were stained with 1% uranyl acetate, dehydrated in an ascending alcohol series, and embedded in Durcupan ACM epoxy resin (Cat. No. 14040). Serial images of the resin embedded samples were acquired by alternating between imaging the block face and shaving off a layer with a diamond knife using a Gatan 3View SBF microtome housed in a Gemini SEM column (Sigma VP, Carl Zeiss) equipped with a Variable Pressure Secondary Electron (VPSE G3) detector. Sets of 200-400 images at 50nm steps, 12k × 12k pixels and 5nm/pixel resolution were obtained, resulting in whole datasets of 60x60µm in the X, Y-plane and 10-20µm in the Z direction. ImageJ Software was used to manually measure g-ratio (ratio of the inner to the outer diameter of the myelin sheath). To determine the g-ratios of myelinated axons in the prefrontal cortex, the total stack of TIFs in each run per animal were first divided evenly into 3 block portions corresponding to beginning, middle, and end of the stack. Ten continuous representative TIFs were selected from each portion (30 total TIFs per animal) and axons were traced using the “polygon selections” tool in ImageJ. Axons in the first TIF of each portion were labeled alphabetically and utilized

as a reference to track the same axon through each block. Inner myelin sheath perimeter was traced first, then the outer myelin sheath perimeter. Diameter was calculated using the perimeter measurement. Axons that were vesiculated, blebbed, detached or oblong myelin sheaths were excluded. For each axon, 5-10 g-ratio measurements taken along the axon were averaged. For each animal, 2-13 axons were averaged.

Flow cytometry

On day 8 p.i., mice were euthanized by CO_2 asphyxiation and perfused with 20-30 mL of sterile PBS. Lungs were collected and processed for flow cytometry as described by Sauer, et al., 2007. In brief, the lungs were chopped with a sterile razor blade, placed in 10ml of collagenase digestion buffer (300U/ ml collagenase type II, 10 ml PBS, 150 ml DNase I of a 10 mg/ml stock) and digested at 37°C for 1h with constant horizontal shaking at 300 r.p.m. (ThermoScientific Max Q 4000). The tissue was passed through a 40µm sieve and cells were washed with 10ml of RPMI media by centrifugation at 400xg for 5 mins. Red blood cells were lysed and the cells were suspended in ice-cold flow cytometry staining buffer (sterile PBS containing 2% FBS) at a concentration of $1x10^6$ cells per 100µl. Cells were stained on ice with fluorophore conjugated antibodies to CD45 (APC; clone 30-F11; ThermoFisher, Cat. No 17-0451-82) and CD11b (FITC; Clone M1/70; ThermoFisher, Cat No. 11-0112-82) for 20 mins. After washing twice in staining buffer, the samples were acquired on a LSRII Flow cytometer (BD). Gates were determined using unstained and single-stained samples obtained from the same tissue of origin and compensation beads respectively. Results were analyzed using FlowJo version 10.6.2 flow cytometry software (De Novo Software).

Data analysis

Lipids were identified with Thermo Scientific software LipidSearch (Version 4.1.30) as previously described[75]. The lipid signals were normalized to whole brain mass and the corresponding internal standard signal responses. For lipid classes without a corresponding internal standard, positive lipid ion signals were normalized to the signal of Ceramide 18:1/12:0 and negative lipid ion species normalized to the signal of Phosphatidylglycerol 14:0/14:0. We only focused on monoisotopic species. LipidSearch software was used to predict the possible fragment ions for lipid species within the precursor ion tolerance using the accurate *m/z* values of the precursor ion. The LipidSearch database are built using the known fragment ions for lipid classes and the intensity pattern based on measured spectra. Identification was done by using the parent ion that was based on the accurate mass of precursor ion with the mass shift tolerance of 5 ppm. Identification of the product ion was based on the accurate mass of precursor ion with mass shift tolerance of 8 ppm and MSMS spectral pattern.

Statistical testing

For lipidomics, differential expression analysis between saline and flu was carried out using the two-sided non-parametric Wilcoxon rank sum test. Python SciPy package was used for calculating the rank sum statistic for each lipid species. Expression fold-change of flu versus saline was computed as a second measure for evaluating differential expression. We required a P-value<0.05 jointly with fold change>2 or fold change<0.5 for significant differential expression. Since only a small number of species were characterized as differentially expressed lipids, the Type 1 error is small and therefore we did not use any P-value correction method and worked with P-values directly obtained from statistical testing. For RT-qPCR analysis, two-tailed Student's t-test was carried out for each gene. A P-value<0.05 was considered statistically significant.

Abbreviations

Acyl Carnitine (AcCa); BisMethyl Phosphatidic Acid (BisMePA); Ceramide (Cer); 2',3' cyclic nucleotide phosphodiesterase (Cnp); DiMethyl Phosphatidyl Ethanolamine (dMePE); Glucosylceramide or galactosylceramide (CerG1, CerG2, CerG3), Cardiolipin (CL); Cholesterol (ChE); Diglyceride (DG); Fatty Acid (FA); Lysophosphatidic Acid (LPA); Lysophosphatidic Choline (LPC); Lysophosphatidyl Ethanolamine (LPE); Lysophosphatidyl Glycerol (LPG); Lysophosphatidic Serine (LPS); Myelin Associated Glycoprotein (Mag); Myelin Basic Protein (Mbp); MePC (Monoether Phosphatidyl Choline); Monogalactosyldiacylglycerol (MGDG); Monoglyceride (MG); Myelin Oligodendrocyte Glycoprotein (Mog); Phosphatidic Acid (PA); Phosphatidyl Choline (PC); Phosphatidyl Ethanolamine (PE); Phosphatidyl Ethanol (PEt); Phosphatidyl Glycerol (PG); Phosphatidyl Inositol (PI); Phosphatidylinositol (3,4,5)-trisphosphate (PI(3,4,5)P3); Proteolipid Protein (PLP); MonoMethyl Phosphatidyl Ethanolamine (PMe); Phosphatidyl Serine (PS); Sphingomyelin (SM); Sphingosine (So); Triradylglyceride (TG); UDP galactosyltransferase 8A (Ugt8a)

Declarations

Acknowledgements: The authors would like to thank Michal Juda for his technical support. This research was funded in part by the USDA National Institute of Food and Agriculture, HATCH Project ILLU-538-932, University of Illinois start-up funds, the National Multiple Sclerosis Society RG 1807-32053, and NIH R21 ES026388 (A.J.S.).

Supported in part by National Institutes of Health Grants R01 GM1155884, R03 DA 04236502, and R21AT010761 (A.D.). J.S.K. was partially supported by the USDA National Institute of Food and Agriculture under the Nutrition and the gut-brain axis: Implications for development and healthy aging grant (2019-38420-28973) to the Division of Nutritional Sciences at the University of Illinois.

Author contributions: A.Y.L. and J.S.K. performed research, analyzed data, and wrote the manuscript. K.S.D., P.D. and S.S. performed research and analyzed data. H.K. provided PLP hybridoma and performed

research. A.J.S., A.D. and R.A.N. secured funding, designed and supervised the research, analyzed data, and wrote the manuscript.

Competing interests: The authors declare no conflict of interest.

References

1 Harris, J. J. & Attwell, D. The Energetics of CNS White Matter. *Journal of Neuroscience* **32**, 356-371, doi:10.1523/jneurosci.3430-11.2012 (2012).

2 Salami, M., Itami, C., Tsumoto, T. & Kimura, F. Change of conduction velocity by regional myelination yields constant latency irrespective of distance between thalamus and cortex. *Proceedings of the National Academy of Sciences* **100**, 6174-6179, doi:10.1073/pnas.0937380100 (2003).

3 Carreiras, M. *et al.* An anatomical signature for literacy. *Nature* **461**, 983-986, doi:10.1038/nature08461 (2009).

4 Fields, R. D. A new mechanism of nervous system plasticity: activity-dependent myelination. *Nature Reviews Neuroscience* **16**, 756-767, doi:10.1038/nrn4023 (2015).

5 Drakesmith, M. *et al.* Mediation of Developmental Risk Factors for Psychosis by White Matter Microstructure in Young Adults With Psychotic Experiences. *JAMA Psychiatry* **73**, 396-406, doi:10.1001/jamapsychiatry.2015.3375 (2016).

6 Dries, D. R. *et al.* Loss of Nicastrin from Oligodendrocytes Results in Hypomyelination and Schizophrenia with Compulsive Behavior. *The Journal of biological chemistry* **291**, 11647-11656, doi:10.1074/jbc.M116.715078 (2016).

7 Owen, M. J., Sawa, A. & Mortensen, P. B. Schizophrenia. *The Lancet* **388**, 86-97, doi:10.1016/s0140-6736(15)01121-6 (2016).

8 Bendlin, B. B. *et al.* White matter in aging and cognition: a cross-sectional study of microstructure in adults aged eighteen to eighty-three. *Developmental neuropsychology* **35**, 257-277, doi:10.1080/87565641003696775 (2010).

9 Prins, N. D. & Scheltens, P. White matter hyperintensities, cognitive impairment and dementia: an update. *Nat Rev Neurol* **11**, 157-165, doi:10.1038/nrneurol.2015.10 (2015).

10 Langdon, D. W. Cognition in multiple sclerosis. *Curr Opin Neurol* **24**, 244-249, doi:10.1097/WCO.0b013e328346a43b (2011).

11 Sacchet, M. D. & Gotlib, I. H. Myelination of the brain in Major Depressive Disorder: An in vivo quantitative magnetic resonance imaging study. *Scientific Reports* **7**, doi:10.1038/s41598-017-02062-y (2017).

12 Bengtsson, S. L. *et al.* Extensive piano practicing has regionally specific effects on white matter development. *Nature Neuroscience* **8**, 1148-1150, doi:10.1038/nn1516 (2005).

13 Scholz, J., Klein, M. C., Behrens, T. E. & Johansen-Berg, H. Training induces changes in white-matter architecture. *Nature neuroscience* **12**, 1370-1371, doi:10.1038/nn.2412 (2009).

14 Forbes, T. A. & Gallo, V. All Wrapped Up: Environmental Effects on Myelination. *Trends Neurosci* **40**, 572-587, doi:10.1016/j.tins.2017.06.009 (2017).

15 Yeung, M. S. *et al.* Dynamics of oligodendrocyte generation and myelination in the human brain. *Cell* **159**, 766-774, doi:10.1016/j.cell.2014.10.011 (2014).

16 McTigue, D. M. & Tripathi, R. B. The life, death, and replacement of oligodendrocytes in the adult CNS. *Journal of neurochemistry* **107**, 1-19, doi:10.1111/j.1471-4159.2008.05570.x (2008).

17 Czopka, T., Ffrench-Constant, C. & Lyons, D. A. Individual oligodendrocytes have only a few hours in which to generate new myelin sheaths in vivo. *Dev Cell* **25**, 599-609, doi:10.1016/j.devcel.2013.05.013 (2013).

18 Aggarwal, S. *et al.* A size barrier limits protein diffusion at the cell surface to generate lipid-rich myelin-membrane sheets. *Dev Cell* **21**, 445-456, doi:10.1016/j.devcel.2011.08.001 (2011).

19 Baron, W. & Hoekstra, D. On the biogenesis of myelin membranes: sorting, trafficking and cell polarity. *FEBS Lett* **584**, 1760-1770, doi:10.1016/j.febslet.2009.10.085 (2010).

20 García-Mateo, N. *et al.* Myelin extracellular leaflet compaction requires apolipoprotein D membrane management to optimize lysosomal-dependent recycling and glycocalyx removal. *Glia* **66**, 670-687, doi:10.1002/glia.23274 (2018).

21 Bergholt, M. S. *et al.* Correlated Heterospectral Lipidomics for Biomolecular Profiling of Remyelination in Multiple Sclerosis. *ACS Cent Sci* **4**, 39-51, doi:10.1021/acscentsci.7b00367 (2018).

22 Fledrich, R. *et al.* Targeting myelin lipid metabolism as a potential therapeutic strategy in a model of CMT1A neuropathy. *Nat Commun* **9**, 3025, doi:10.1038/s41467-018-05420-0 (2018).

23 Bosio, A., Binczek, E. & Stoffel, W. Functional breakdown of the lipid bilayer of the myelin membrane in central and peripheral nervous system by disrupted galactocerebroside synthesis. *Proc Natl Acad Sci U S A* **93**, 13280-13285, doi:10.1073/pnas.93.23.13280 (1996).

24 Coetzee, T. *et al.* Myelination in the absence of galactocerebroside and sulfatide: normal structure with abnormal function and regional instability. *Cell* **86**, 209-219, doi:10.1016/s0092-8674(00)80093-8 (1996).

25 Dantzer, R., O'Connor, J. C., Freund, G. G., Johnson, R. W. & Kelley, K. W. From inflammation to sickness and depression: when the immune system subjugates the brain. *Nat Rev Neurosci* **9**, 46-56, doi:10.1038/nrn2297 (2008).

26 Surana, P. *et al.* Neurological complications of pandemic influenza A H1N1 2009 infection: European case series and review. *European journal of pediatrics* **170**, 1007-1015, doi:10.1007/s00431-010-1392-3 (2011).

27 Rogers, J. P. *et al.* Psychiatric and neuropsychiatric presentations associated with severe coronavirus infections: a systematic review and meta-analysis with comparison to the COVID-19 pandemic. *Lancet Psychiatry* **7**, 611-627, doi:10.1016/s2215-0366(20)30203-0 (2020).

28 Kępińska, A. P. *et al.* Schizophrenia and Influenza at the Centenary of the 1918-1919 Spanish Influenza Pandemic: Mechanisms of Psychosis Risk. *Front Psychiatry* **11**, 72, doi:10.3389/fpsyt.2020.00072 (2020).

29 Hoogland, I. C., Houbolt, C., van Westerloo, D. J., van Gool, W. A. & van de Beek, D. Systemic inflammation and microglial activation: systematic review of animal experiments. *Journal of neuroinflammation* **12**, 114, doi:10.1186/s12974-015-0332-6 (2015).

30 Sadasivan, S., Zanin, M., O'Brien, K., Schultz-Cherry, S. & Smeyne, R. J. Induction of microglia activation after infection with the non-neurotropic A/CA/04/2009 H1N1 influenza virus. *PloS one* **10**, e0124047, doi:10.1371/journal.pone.0124047 (2015).

31 Ji, P., Schachtschneider, K. M., Schook, L. B., Walker, F. R. & Johnson, R. W. Peripheral viral infection induced microglial sensome genes and enhanced microglial cell activity in the hippocampus of neonatal piglets. *Brain, behavior, and immunity* **54**, 243-251, doi:10.1016/j.bbi.2016.02.010 (2016).

32 Jurgens, H. A., Amancherla, K. & Johnson, R. W. Influenza Infection Induces Neuroinflammation, Alters Hippocampal Neuron Morphology, and Impairs Cognition in Adult Mice. *The Journal of Neuroscience* **32**, 3958, doi:10.1523/JNEUROSCI.6389-11.2012 (2012).

33 Peferoen, L., Kipp, M., van der Valk, P., van Noort, J. M. & Amor, S. Oligodendrocyte-microglia cross-talk in the central nervous system. *Immunology* **141**, 302-313, doi:10.1038/nn.326310.1111/imm.12163 (2014).

34 Blackmore, S. *et al.* Influenza infection triggers disease in a genetic model of experimental autoimmune encephalomyelitis. *Proceedings of the National Academy of Sciences* **114**, E6107-E6116, doi:10.1073/pnas.1620415114 (2017).

35 Poitelon, Y., Kopec, A. M. & Belin, S. Myelin Fat Facts: An Overview of Lipids and Fatty Acid Metabolism. *Cells* **9**, doi:10.3390/cells9040812 (2020).

36 Lüders, K. A. *et al.* Maintenance of high proteolipid protein level in adult central nervous system myelin is required to preserve the integrity of myelin and axons. *Glia* **67**, 634-649, doi:10.1002/glia.23549 (2019).

37 Klugmann, M. *et al.* Assembly of CNS myelin in the absence of proteolipid protein. *Neuron* **18**, 59-70, doi:10.1016/s0896-6273(01)80046-5 (1997).

38 Skripuletz, T. *et al.* Cortical demyelination is prominent in the murine cuprizone model and is strain-dependent. *The American journal of pathology* **172**, 1053-1061, doi:ajpath.2008.070850 [pii]10.2353/ajpath.2008.070850 [doi] (2008).

39 Liddelow, S. A. *et al.* Neurotoxic reactive astrocytes are induced by activated microglia. *Nature* **541**, 481-487, doi:10.1038/nature21029 (2017).

40 Zhang, Y. *et al.* An RNA-sequencing transcriptome and splicing database of glia, neurons, and vascular cells of the cerebral cortex. *J Neurosci* **34**, 11929-11947, doi:10.1523/jneurosci.1860-14.2014 (2014).

41 Lein, E. S. *et al.* Genome-wide atlas of gene expression in the adult mouse brain. *Nature* **445**, 168-176, doi:10.1038/nature05453 (2007).

42 Schaum, N. *et al.* Single-cell transcriptomics of 20 mouse organs creates a Tabula Muris. *Nature* **562**, 367-372, doi:10.1038/s41586-018-0590-4 (2018).

43 Crespo, O. *et al.* Tyrosine kinase inhibitors ameliorate autoimmune encephalomyelitis in a mouse model of multiple sclerosis. *J Clin Immunol* **31**, 1010-1020, doi:10.1007/s10875-011-9579-6 (2011).

44 Martínez-Muriana, A. *et al.* CSF1R blockade slows the progression of amyotrophic lateral sclerosis by reducing microgliosis and invasion of macrophages into peripheral nerves. *Scientific Reports* **6**, 25663, doi:10.1038/srep25663 (2016).

45 Olmos-Alonso, A. *et al.* Pharmacological targeting of CSF1R inhibits microglial proliferation and prevents the progression of Alzheimer's-like pathology. *Brain : a journal of neurology* **139**, 891-907, doi:10.1093/brain/awv379 (2016).

46 Gerber, Y. N. *et al.* CSF1R Inhibition Reduces Microglia Proliferation, Promotes Tissue Preservation and Improves Motor Recovery After Spinal Cord Injury. *Frontiers in cellular neuroscience* **12**, 368, doi:10.3389/fncel.2018.00368 (2018).

47 Yan, X., Maixner, D. W., Li, F. & Weng, H. R. Chronic pain and impaired glial glutamate transporter function in lupus-prone mice are ameliorated by blocking macrophage colony-stimulating factor-1 receptors. *J Neurochem* **140**, 963-976, doi:10.1111/jnc.13952 (2017).

48 Chalmers, S. A. *et al.* CSF-1R inhibition attenuates renal and neuropsychiatric disease in murine lupus. *Clinical immunology (Orlando, Fla.)* **185**, 100-108, doi:10.1016/j.clim.2016.08.019 (2017).

49 Young, K. M. *et al.* Oligodendrocyte dynamics in the healthy adult CNS: evidence for myelin remodeling. *Neuron* **77**, 873-885, doi:10.1016/j.neuron.2013.01.006 (2013).

50 Snaidero, N. *et al.* Myelin membrane wrapping of CNS axons by PI(3,4,5)P3-dependent polarized growth at the inner tongue. *Cell* **156**, 277-290, doi:10.1016/j.cell.2013.11.044 (2014).

51 Liu, J. *et al.* Impaired adult myelination in the prefrontal cortex of socially isolated mice. *Nat Neurosci* **15**, 1621-1623, doi:10.1038/nn.3263 (2012).

52 Lehmann, M. L., Weigel, T. K., Elkahloun, A. G. & Herkenham, M. Chronic social defeat reduces myelination in the mouse medial prefrontal cortex. *Scientific Reports* **7**, 46548, doi:10.1038/srep46548 (2017).

53 Bonnefil, V. *et al.* Region-specific myelin differences define behavioral consequences of chronic social defeat stress in mice. *Elife* **8**, doi:10.7554/eLife.40855 (2019).

54 Plieger, T., Melchers, M., Montag, C., Meermann, R. & Reuter, M. Life stress as potential risk factor for depression and burnout. *Burnout Research* **2**, 19-24, doi:https://doi.org/10.1016/j.burn.2015.03.001 (2015).

55 Cathomas, F. *et al.* Oligodendrocyte gene expression is reduced by and influences effects of chronic social stress in mice. *Genes Brain Behav* **18**, e12475, doi:10.1111/gbb.12475 (2019).

56 Aston, C., Jiang, L. & Sokolov, B. P. Transcriptional profiling reveals evidence for signaling and oligodendroglial abnormalities in the temporal cortex from patients with major depressive disorder. *Mol Psychiatry* **10**, 309-322, doi:10.1038/sj.mp.4001565 (2005).

57 Dhar, A. K. & Barton, D. A. Depression and the Link with Cardiovascular Disease. *Front Psychiatry* **7**, 33, doi:10.3389/fpsyt.2016.00033 (2016).

58 Miller, A. H. & Raison, C. L. The role of inflammation in depression: from evolutionary imperative to modern treatment target. *Nat Rev Immunol* **16**, 22-34, doi:10.1038/nri.2015.5 (2016).

59 Dantzer, R. & Kelley, K. W. Twenty years of research on cytokine-induced sickness behavior. *Brain Behav Immun* **21**, 153-160, doi:10.1016/j.bbi.2006.09.006 (2007).

60 Udina, M. *et al.* Interferon-induced depression in chronic hepatitis C: a systematic review and meta-analysis. *J Clin Psychiatry* **73**, 1128-1138, doi:10.4088/JCP.12r07694 (2012).

61 Blank, T. *et al.* Brain Endothelial- and Epithelial-Specific Interferon Receptor Chain 1 Drives Virus-Induced Sickness Behavior and Cognitive Impairment. *Immunity* **44**, 901-912,

doi:10.1016/j.immuni.2016.04.005 (2016).

62 Buscham, T. J., Eichel, M. A., Siems, S. B. & Werner, H. B. Turning to myelin turnover. *Neural Regen Res* **14**, 2063-2066, doi:10.4103/1673-5374.262569 (2019).

63 Saadat, L. *et al.* Absence of oligodendroglial glucosylceramide synthesis does not result in CNS myelin abnormalities or alter the dysmyelinating phenotype of CGT-deficient mice. *Glia* **58**, 391-398, doi:10.1002/glia.20930 (2010).

64 Schwarz, E. *et al.* High throughput lipidomic profiling of schizophrenia and bipolar disorder brain tissue reveals alterations of free fatty acids, phosphatidylcholines, and ceramides. *J Proteome Res* **7**, 4266-4277, doi:10.1021/pr800188y [doi] (2008).

65 Wood, P. L., Tippireddy, S., Feriante, J. & Woltjer, R. L. Augmented frontal cortex diacylglycerol levels in Parkinson's disease and Lewy Body Disease. *PLoS One* **13**, e0191815, doi:10.1371/journal.pone.0191815 (2018).

66 Yu, Q. *et al.* Lipidome alterations in human prefrontal cortex during development, aging, and cognitive disorders. *Mol Psychiatry* **25**, 2952-2969, doi:10.1038/s41380-018-0200-8 (2020).

67 Lydic, T. A. & Goo, Y. H. Lipidomics unveils the complexity of the lipidome in metabolic diseases. *Clin Transl Med* **7**, 4, doi:10.1186/s40169-018-0182-9 (2018).

68 Gopalakrishnan, G. *et al.* Lipidome and proteome map of myelin membranes. *J Neurosci Res* **91**, 321-334, doi:10.1002/jnr.23157 (2013).

69 Ziemka-Nalecz, M. *et al.* Impact of neonatal hypoxia-ischaemia on oligodendrocyte survival, maturation and myelinating potential. *J Cell Mol Med* **22**, 207-222, doi:10.1111/jcmm.13309 (2018).

70 Yang, L. Q., Chen, M., Zhang, J. L., Ren, D. L. & Hu, B. Hypoxia Delays Oligodendrocyte Progenitor Cell Migration and Myelin Formation by Suppressing Bmp2b Signaling in Larval Zebrafish. *Front Cell Neurosci* **12**, 348, doi:10.3389/fncel.2018.00348 (2018).

71 Doan, V. *et al.* Abbreviated exposure to cuprizone is sufficient to induce demyelination and oligodendrocyte loss. *J Neurosci Res* **91**, 363-373, doi:10.1002/jnr.23174 (2013).

72 Epp, J. R. *et al.* Optimization of CLARITY for Clearing Whole-Brain and Other Intact Organs. *eNeuro* **2**, doi:10.1523/eneuro.0022-15.2015 (2015).

73 Larocca, J. N. & Norton, W. T. Isolation of myelin. *Curr Protoc Cell Biol* **Chapter 3**, Unit3.25, doi:10.1002/0471143030.cb0325s33 (2007).

74 BLIGH, E. G. & DYER, W. J. A rapid method of total lipid extraction and purification. *Can J Biochem Physiol* **37**, 911-917, doi:10.1139/o59-099 (1959).

75 Roy, J., Dibaeinia, P., Fan, T. M., Sinha, S. & Das, A. Global analysis of osteosarcoma lipidomes reveal altered lipid profiles in metastatic versus nonmetastatic cells. *Journal of lipid research* **60**, 375-387, doi:10.1194/jlr.M088559 (2019).

Figures

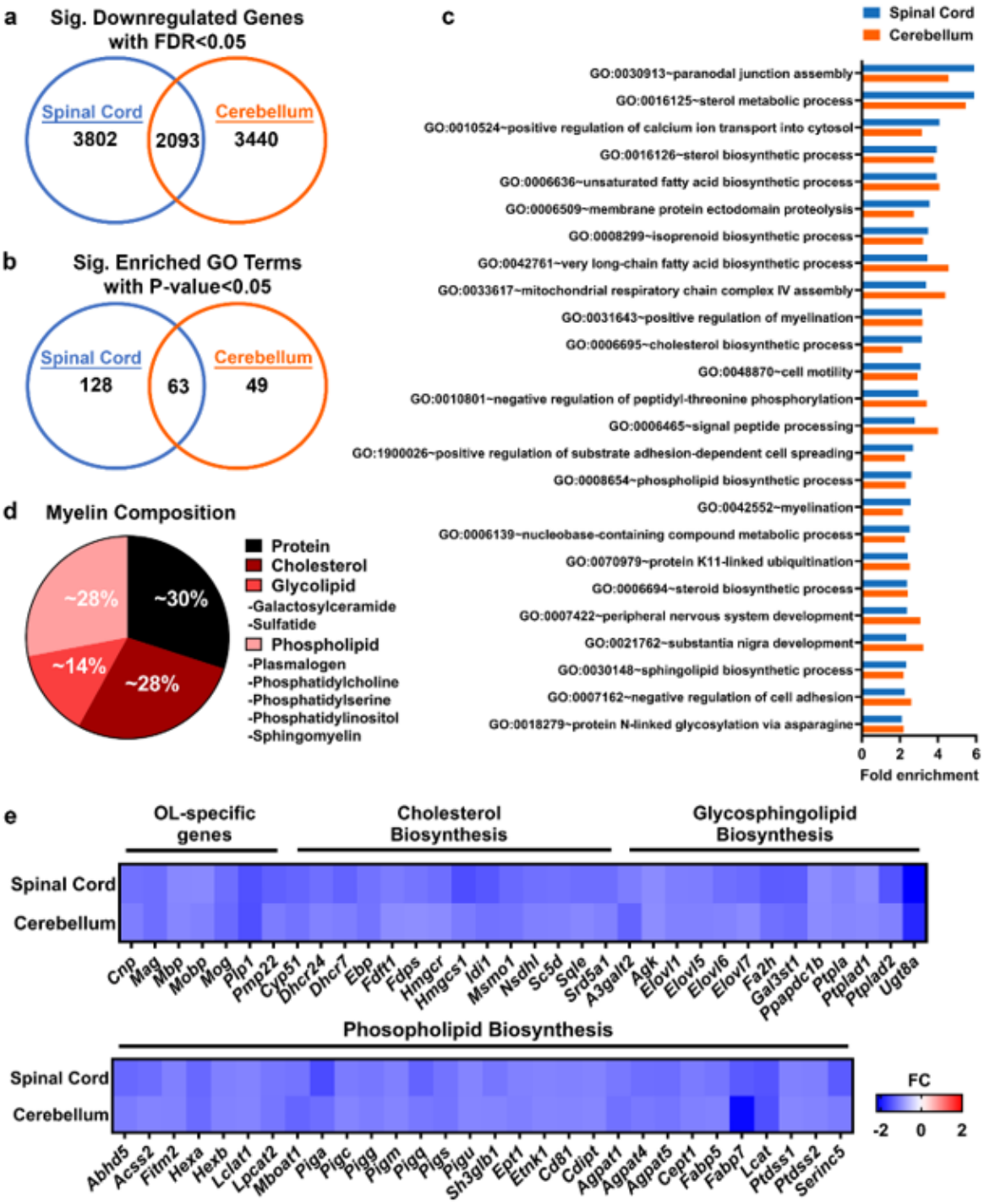

Figure 1

RNA sequencing reveals influenza alters lipid biosynthesis and myelination pathways of the cerebellum and spinal cord transcriptome. (a) Overlap of significantly downregulated genes between the spinal cord and cerebellum of flu-infected mice compared to saline-inoculated mice at day 8 p.i. (n=7-8, $p<0.05$, FDR<0.05). (b) Overlap of significantly enriched Gene Ontology (GO) terms identified with DAVID Bioinformatics Resources in the spinal cord and cerebellum corresponding to significantly downregulated genes of Fig. 1a. (c) Fold enrichment of the 25 most highly enriched GO pathways shared between the spinal cord and cerebellum at day 8 p.i. (d) Percentage breakdown of major myelin constituents (modified from Poitelon et al., 2020)35. (e) Fold change (FC) expression of genes encoding myelin proteins and enzymes involved in cholesterol biosynthesis, glycosphingolipid biosynthesis, and phospholipid biosynthesis of both the spinal cord and cerebellum of infected mice compared to controls (n=7-8, $p<0.05$, FDR<0.05). Data are from Blackmore et al., 2017 (accession no. GSE96870)34.

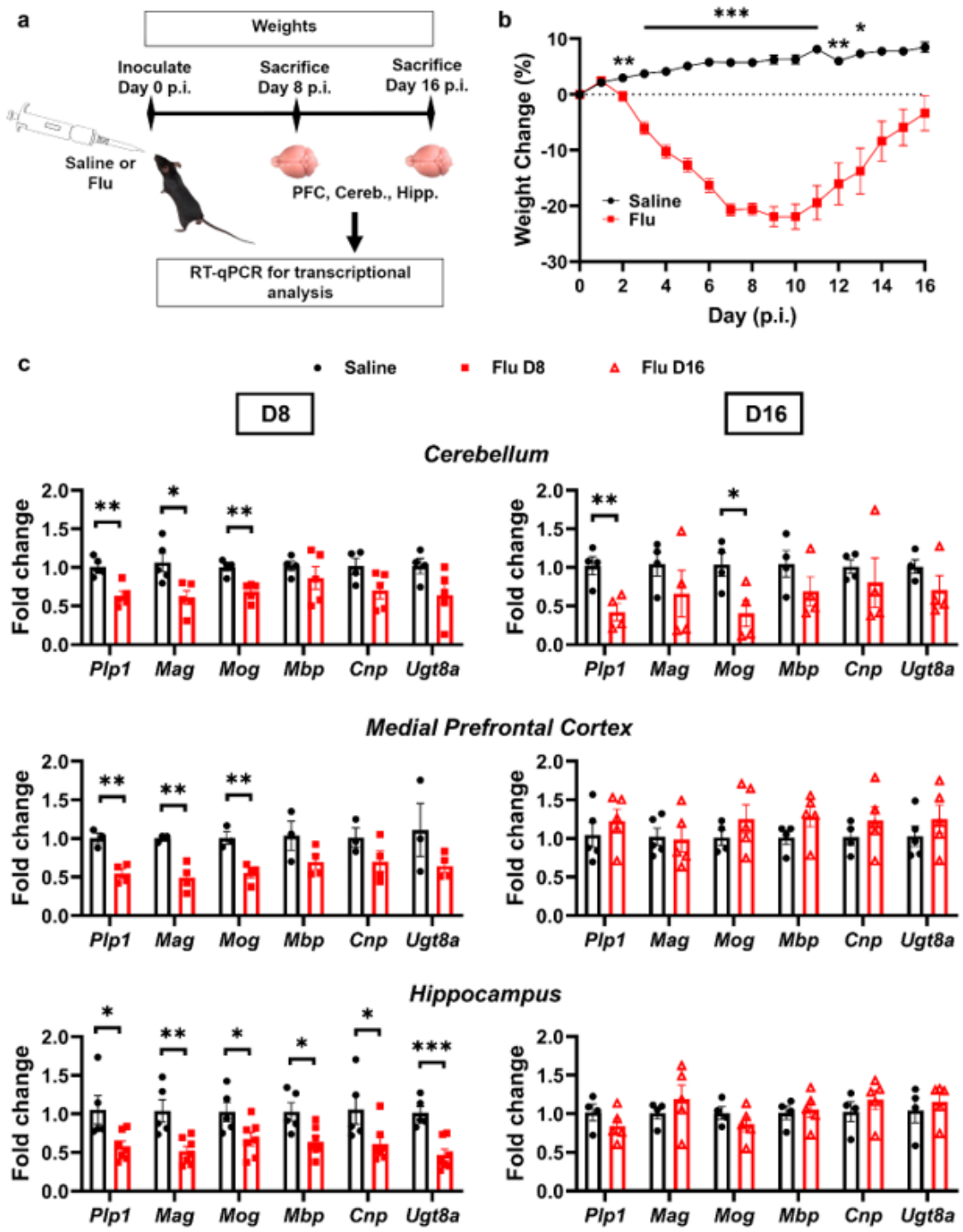

Figure 2

Influenza infection decreases OL-specific transcripts in multiple regions of the brain with region-specific recovery of transcripts by day 16 p.i. (a) Experimental design to uncover regional transcriptional changes to myelin-related genes in the brain at days 8 and 16 p.i. (b) Percent daily weight change (n=18-22 animals per condition, pooled from all experiments) (c) RT-qPCR analysis of myelination genes in the cerebellum, prefrontal cortex, and hippocampus of adult mice at days 8 and 16 p.i. (n=3-7 animals per

condition, two-tailed Student's t test). Data are presented as mean ± SEM. P-value significance *<0.05, **<0.01, ***<0.001.

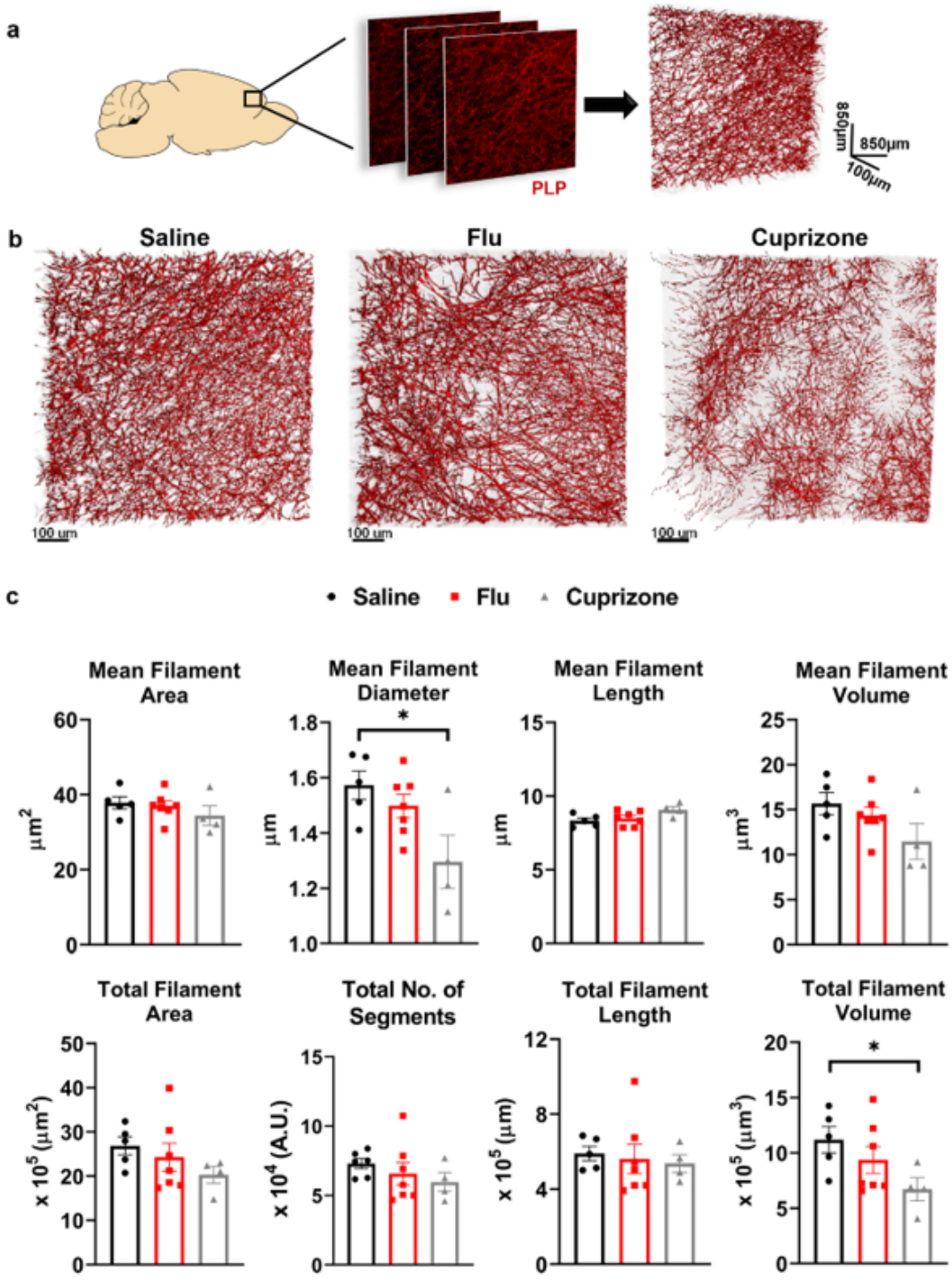

Figure 3

Influenza infection does not significantly alter PLP levels in the mPFC. (a) Schematic overview of immunofluorescence technique to evaluate PLP in the mPFC. Dimension bar not drawn to scale. (b) Representative 3D renderings of PLP-stained mPFC tissue of saline, flu, and cuprizone treatment groups.

(c) Select measures from Imaris data output related to known biological attributes of myelinated fibers of saline, flu, and cuprizone treatment groups at day 8 p.i. (n=4-7 animals per condition). Data are presented as mean ± SEM. P-value significance *<0.05.

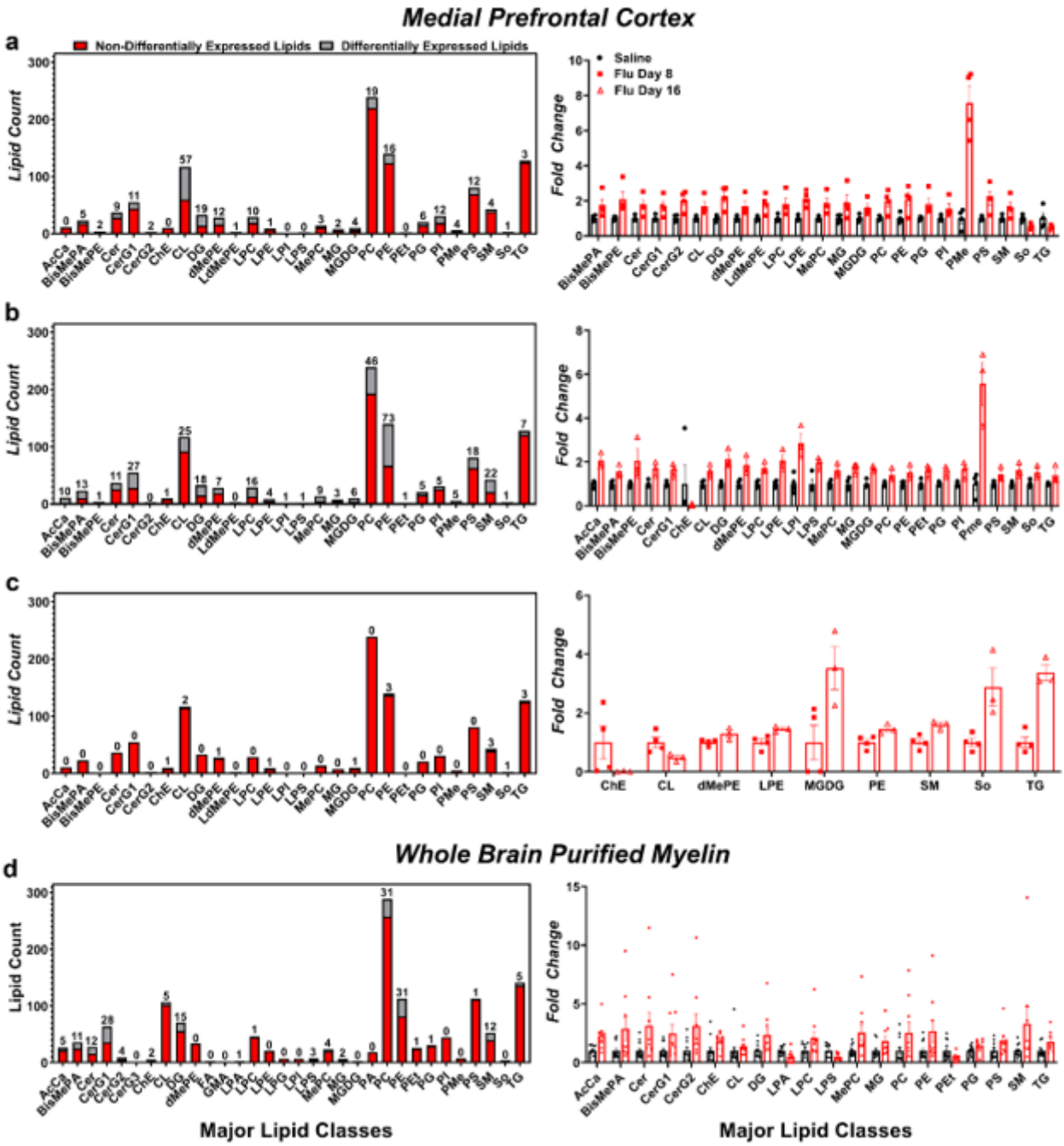

Figure 4

Lipidomics analyses reveals lipid changes in purified myelin. (a-c) Left; Differential expression of lipid species between saline (n=4), flu day 8 (n=4), and flu day 16 (n=3) in the mPFC. 2-3 animals were pooled for each mPFC sample. Values above histogram represent number of individual lipid species unique to its respective major lipid class. Right; Differentially expressed lipids (p<0.05) of overall major lipid classes

plotted as fold change of saline, flu day 8, and flu day 16. (d) Differential expression of lipid species between saline (n=12), and flu day 8 (n=12) in purified myelin isolated from whole brain. Differentially expressed lipids ($p<0.05$) of overall major lipid classes plotted as fold change of saline and flu day 8.

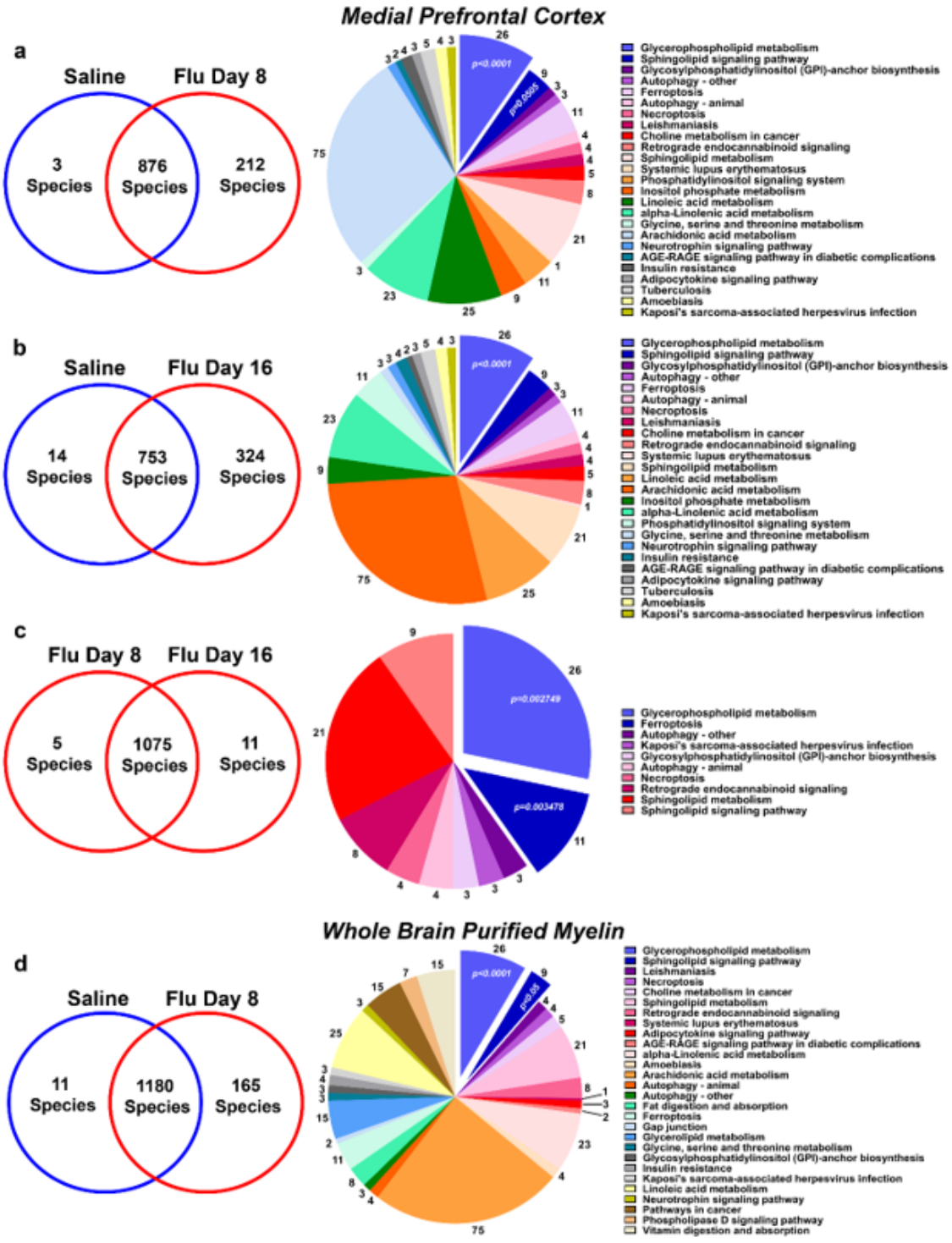

Figure 5

LIPEA Bioinformatics reveal changes in signaling pathways. (a-c) Left; number of unique lipids in saline, flu day 8, or flu day 16 groups in the mPFC. Right; Differentially expressed lipids with biological pathways

analyzed by LIPEA with Bonferroni correction. Values represent number of lipid species involved in each pathway. (d) Left; number of unique lipids in saline or flu day 8 in purified myelin isolated from whole brain. Right; Differentially expressed lipids with biological pathways analyzed by LIPEA with Bonferroni correction. P-value significance is as follows * < 0.05, ** < 0.01, *** < 0.001, **** < 0.0001.

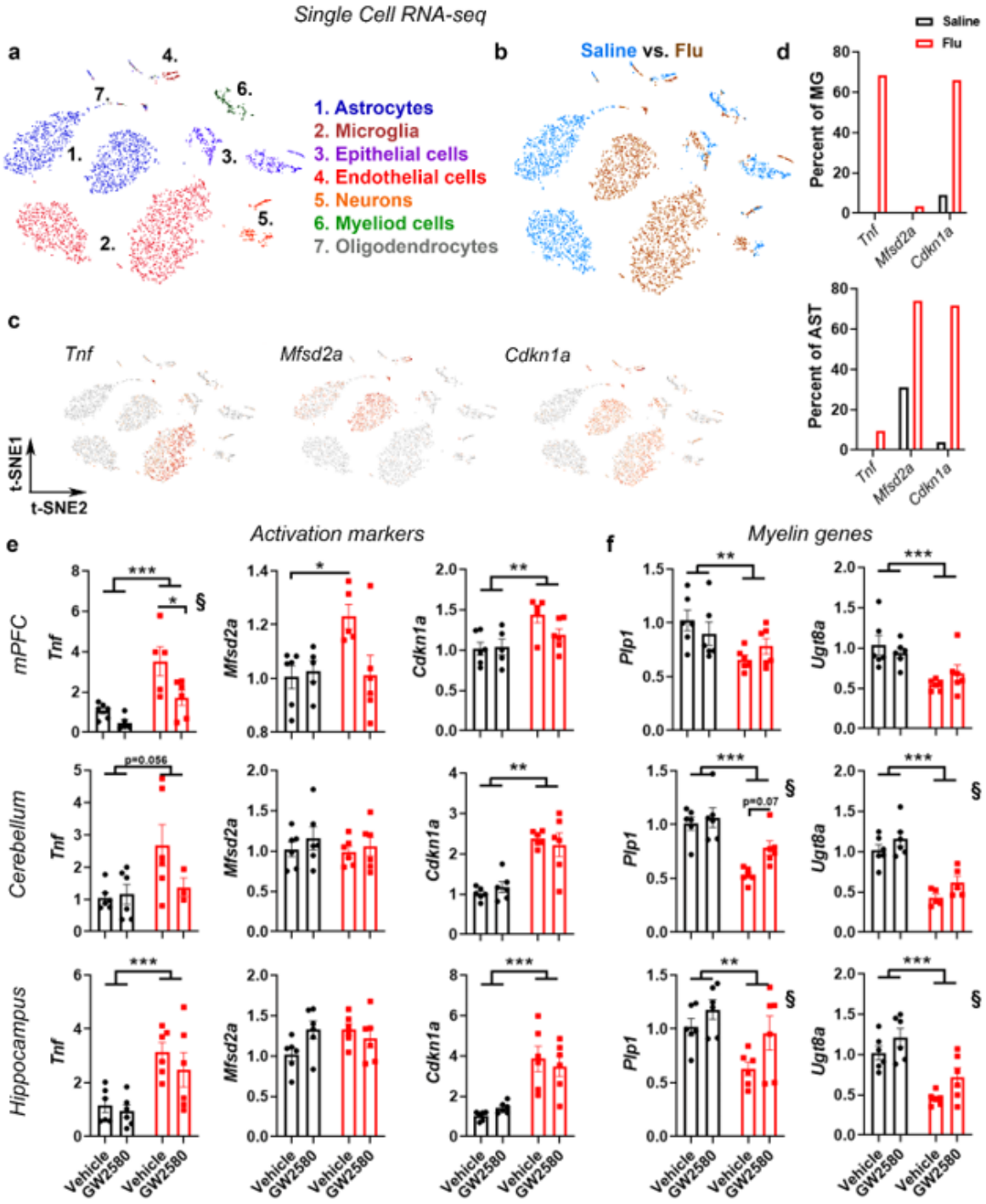

Figure 6

Infection-induced changes to OL-specific transcripts are partially attenuated following treatment with a CSF1R antagonist. (a-d), C57BL/6J mice were inoculated with saline (n=1) or influenza (n=1; 1.0 HAU). At day 8 p.i. brain cells were isolated and subjected to single cell (sc)RNA-seq (a-b), t-distributed stochastic neighbor embedding (t-SNE) plots showing identified cell types (a) and effect of influenza infection (b). (c-d) Upregulated genes associated with infection-induced changes to microglia (Tnf; left), astrocytes (Mfsd2a; middle) or all cell types (Cdkn1a; right). Results are from 4,142 total cells (Saline, n=1894; Flu, n=2248). (e-f) C57BL/6J mice were treated with vehicle or the CSF1R inhibitor GW2580 (80mg/kg/d) by oral gavage for 8 days then inoculated with saline or influenza (n=6 per group). Brain regions were micro-dissected at day 8 p.i. and gene expression analyzed. Effects of infection and treatment on expression of inflammatory (e) and OL-specific (f) genes in the mPFC (top), cerebellum (middle) and hippocampus (bottom) are shown. Results are means ± S.E. Individual mice are depicted. Significance was determined by two-way ANOVA. Bars represent main effect of infection. P-value significance *<0.05, **<0.01, ***<0.001. Main effect of treatment is indicated by the symbol §.

Supplementary Files

This is a list of supplementary files associated with this preprint. Click to download.

- 2SupplementaryMaterialCOMBINEDFINAL.pdf
- SupplementaryMovie1.gif
- SupplementaryMovie2.gif
- SupplementaryMovie3.gif
- SupplementaryData1.xlsx